From atmospheric water isotopes measurement to firn core interpretation in Adelie Land: A case study for isotope-enabled atmospheric models in Antarctica

Christophe Leroy-Dos Santos[1,2], Elise Fourré[1], Cécile Agosta[1], Mathieu Casado[1], Alexandre Cauquoin[3], Martin Werner[4], Benedicte Minster[1], Frédéric Prié[1], Olivier Jossoud[1], Leila Petit[1], and Amaelle Landais[1]

[1]Laboratoire des Sciences du Climat et de l'Environnement, LSCE-IPSL, CEA-CNRS-UVSQ, Université Paris-Saclay, Gif-sur-Yvette, France
[2]Centre for Environmental and Marine Studies (CESAM), Department of Physics, University of Aveiro, Portugal
[3]Institute of Industrial Science (IIS), The University of Tokyo, Kashiwa, Japan
[4]Alfred Wegener Institute (AWI), Helmholtz Centre for Polar and Marine Research, Bremerhaven, Germany

Correspondence: Christophe Leroy-Dos Santos (christophe.leroy@lsce.ipsl.fr)

Abstract.

In a context of global warming and sea level rise acceleration, it is key to estimate the evolution of the atmospheric hydrological cycle and temperature in polar regions, which directly influence the surface mass balance of the Arctic and Antarctic ice sheets. Direct observations are available from satellite data for the last 40 years and a few weather data since the 50's in
5   Antarctica. One of the best ways to access longer records is to use climate proxies in firn or ice cores. The water isotopic composition in these cores is widely used to reconstruct past temperature variations.

We need to progress in our understanding of the influence of the atmospheric hydrological cycle on the water isotopic composition of ice-core. First, we present a 2-year long time series of vapor and precipitation isotopic composition measurement at Dumont d'Urville station, in Adélie Land. We characterize diurnal variations of meteorological parameters (temperature,
10   atmospheric water mixing ratio (hereafter humidity) and $\delta^{18}O$) for the different seasons and determine the evolution of key relationships ($\delta^{18}O$ versus temperature or humidity) along the year: we find that the temperature vs $\delta^{18}O$ relationship is dependent on synoptic events dynamics in winter contrary to summer. Then, this data set is used to evaluate the Atmospheric General Circulation Model ECHAM6-wiso (model version with embedded water stable isotopes) in a coastal region of Adélie Land where local conditions are controlled by strong katabatic winds which directly impact the isotopic signal. We show that a
15   combination of continental (79%) and oceanic (21%) grid cells leads model outputs (temperature, humidity and $\delta^{18}O$) to nicely fit the observations, at different time scales (i.e. seasonal to synoptic). Therefore we demonstrate the added value of long-term water vapor isotopic composition records for model evaluation.

Then, as a clear link is found between the isotopic composition of water vapor and precipitation, we assess how isotopic models can help interpret short firn cores. In fact, a virtual firn core built from ECHAM-wiso outputs explains much more
20   of the variability observed in S1C1 isotopic record than a virtual firn core built from temperature only. Yet, deposition and post-deposition effects strongly affects the firn isotopic signal and probably account for most of the remaining misfits between archived firn signal and virtual firn core based on atmospheric modeling.

1 Introduction

East Antarctica is the biggest fresh water reservoir on Earth (Smith and Evans, 2007). In a context of global warming, it is key to monitor and anticipate the surface mass balance (SMB) of this region and its link with climate change. Adélie Land is part of the Wilkes Land Coast, a region that is at the boundary between the eastern part of the Antarctic plateau and the Indian ocean. Recent studies based on remote observations, reanalysis or CMIP5 models disagree on the recent evolution of temperature in this region (Wang et al., 2020; Retamales-Muñoz et al., 2019; Stenni et al., 2017), showing that it is complicated to determine how it is impacted by global warming.

Antarctica climate and ice sheet altitude evolution have been measured for four decades based on remote sensing and show an increasing mass loss in Wilkes Land (Rignot et al., 2019). These reconstructions require calibrations or evaluation with ground based measurements but weather stations and direct observations of surface mass balance are sparse (Favier et al., 2013; Wang et al., 2021). Global reanalysis data are suitable for studying climate variability, but these products have only been reliable in the data-scarce Antarctic region since 1979, when they began assimilating satellite data (Marshall et al., 2022). For periods older than 40 years, Antarctic climate reconstructions rely on a few weather stations installed in the 50's (Fogt et al., 2016) or on the interpretation of climate proxies. Water isotope measurements in firn and ice cores are key tools to provide reconstruction of past climate and atmospheric water cycle over the last centuries and millennia (Jouzel et al., 2013; Stenni et al., 2017). They have been extensively used for past temperature reconstructions in continental Antarctica where water isotopic depletion can be related to temperature decrease through increased distillation along the atmospheric moisture path from evaporative regions to the precipitation sites of interest (Jouzel et al., 2007; Stenni et al., 2011). The interpretation of water isotope records in coastal Antarctica is more difficult because distillation is not the sole dominant influence on the water isotopic signal. Local effects of ocean evaporation itself influenced by the presence of sea ice, katabatic wind direction and speed, remobilisation or sublimation of surface snow may also have a strong effect on the water isotopic composition of the deposited snow and hence on the archived signal (Ekaykin et al., 2002; Casado et al., 2018). While these effects prevent a simple interpretation of water isotopes as temperature proxy, they open the way to the use of these tracers to better constrain the past atmospheric water cycle.

In fact, recent studies have shown that isotopic signals recorded in coastal ice or firn cores are poorly correlated to surface temperature (Goursaud et al., 2017, 2019) or to SMB (Schlosser et al., 2014). This is confirmed by Altnau et al. (2015) who observed weaker relationship between SMB and δ^{18}O for coastal firn cores in comparison to inland drilling sites with a 76 firn core dataset in Dronning Maud Land. Finally, these studies point out the need to take into account the influences of atmospheric dynamics and local processes, in addition to the classical thermodynamics part on isotopic signals. For instance, Sinclair et al. (2014) studied sea ice variations in the Ross Sea using d-excess signal, a second order parameter reflecting evaporative conditions, coupled with chemical indicators in a core from Whitehall Glacier. This study attributes the observed variations to enhanced southerly winds and an increased advection of sea ice to the north showing regional dynamics influences. Also, from shallow firn cores drilled in Fimbul Ice Shelf in western Dronning Maud Land, Vega et al. (2016) suggest that d-excess reflects the effect of seasonal moisture transport changes. Furthermore, other ice core interpretation techniques, such as virtual

firn cores (Sime et al., 2011; Casado et al., 2020) that take into account the intermittency of precipitation and isotope diffusion in firn, encourage the use of isotope-enabled models in order to consider other processes than temperature that affect isotopic signal (Sime et al., 2011; Casado et al., 2020). For example, Goursaud et al. (2018) demonstrated how ECHAM5-wiso could be valuable to investigate the dynamics of water stable isotope composition in precipitation in regard to different locations or seasons.

We build on these previous studies and aim at better constraining the isotopic signal of water vapor and precipitation in coastal sites to improve the interpretation of firn and ice core archives. This can be achieved by measuring the isotopic composition of precipitation and water vapor on site in order to understand local dynamics influences and using atmospheric general circulation models (AGCMs) equipped with water vapor isotopes outputs that already include various processes linked to atmospheric dynamics. For example, large diurnal cycles observed in the isotopic composition of water vapor at Dome C were associated with atmospheric regimes demonstrating the impact of local meteorological processes on the isotopic signal (Casado et al., 2016). At Kohnen, Ritter et al. (2016) showed that mean diurnal cycles amplitude simulated by AGCMs (ECHAM5-wiso and LMDZ5Aiso) is lower than observed. In coastal regions, it has been observed that the isotopic signature of maritime air mass contrasts with depleted cold glacial air mass at Syowa station (Kurita et al., 2016) while in Adélie Land, a first summer campaign of measurements made it possible to understand the influence of katabatic wind dynamics on the diurnal isotopic cycle (Bréant et al., 2019). Also, a two-year data series at Neumayer station III was used to associate isotopic signal in water vapor to air masses origin through back trajectory simulations analyses (Bagheri Dastgerdi et al., 2020).

Here we present a long-term study of continuous isotopic measurement of water vapor and precipitation at Dumont d'Urville (DDU). First, we present our instrumental set-up and the 2-year isotopic series observed at DDU. Then, we show the ECHAM6-wiso output at DDU geographical position and evaluate the model performance. Finally, we discuss the added value of an isotope-enabled model for ice-core interpretation in coastal regions by comparing an ECHAM6-wiso based virtual firn core to a firn core drilled close to DDU and presented in a previous study (Goursaud et al., 2017).

2 Materials and Methods

2.1 Observations

2.1.1 Water vapor isotopic composition

A Picarro analyzer (L2130-i) was installed in December 2018 in Adélie Land, at the coastal DDU station (Fig. 1) to monitor the isotopic composition of atmospheric water vapor. We used the same configuration as in Bréant et al. (2019), i.e. an inlet is positioned 1 meter above the shelter roof, 6 meters above ground level, roughly 30 meters above sea level (a.s.l.). This inlet is connected to the isotopic analyzer by a heated and insulated perfluoroalkoxy (PFA) tube. The inlet is covered by a Gelman Zefluor 0.5 μm filter to prevent any inflow of precipitation, blowing snow or penguins' feathers. Continuous measurement of the isotopic composition of atmospheric water vapor is still running to date. Here we present the first two years of measurement, from 1 January 2019 to 31 December 2020.
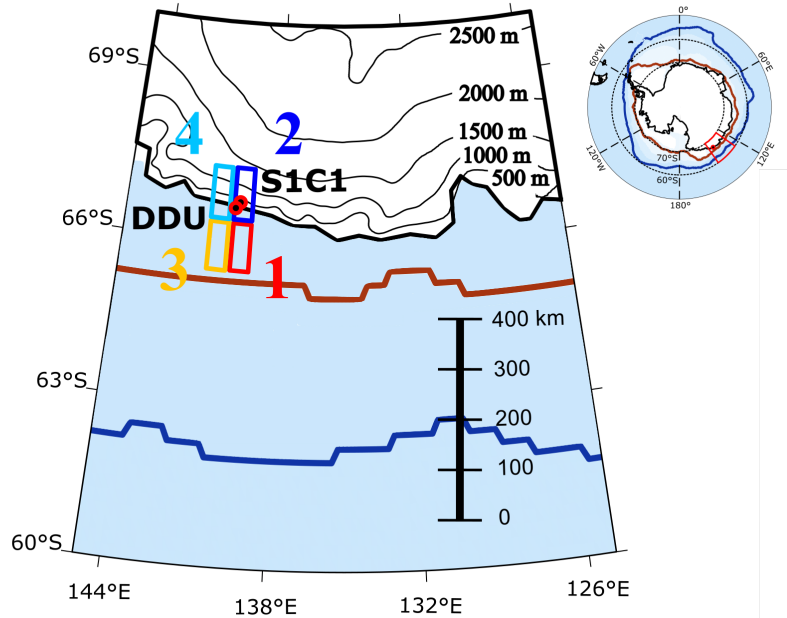
3

Figure 1. Adelie land map with Dumont d'Urville scientific station (located on Petrel Island, 5 km from the coast) and S1C1 drilling site (10 km inland) indicated by red dots. Black contours represent the topography, bold red and blue lines represent the sea-ice extent, respectively in March and October, defined as areas with a minimum sea-ice fraction of 0.15 from the ERA5 reanalysis over the period 1979-2020, as in Ding et al. (2017). Labelled (from #1 to #4) and colored (in red, blue, orange and light blue) rectangles represent closest ECHAM6-wiso grid cells to DDU.

The laser spectrometer measures molecular water vapor mixing ratio (in ppmv), hereafter called humidity, and water vapor $\delta^{18}O$ and δD. The raw datasets have been calibrated and corrected following the protocol outlined in previous studies (Tremoy et al., 2011; Bonne et al., 2014; Steen-Larsen et al., 2014) and described below.

Humidity values have been compared to independent measurements from Meteo France weather station at DDU (Fig. S1 in Supplement). The comparison shows a robust linear relationship between both measurements over the 2-year period (coefficient of determination, hereafter called R^2, equal to 0.99 and slope of 0.98). In the following, we only display raw humidity data from Picarro without any correction.

The $\delta^{18}O$ and δD series were calibrated following the approach described in Leroy-Dos Santos et al. (2020). Three main corrections were applied: 1) the influence of humidity on $\delta^{18}O$ and δD measurement, 2) the difference between the measured values and the true isotopic values, and 3) the temporal drift of the instrument. For the calibration procedure, we used both a specifically designed low humidity level generator described in Leroy-Dos Santos et al. (2021) and a standard delivery module

100 (SDM) associated with a Picarro brand vaporizer for higher humidity values. For consistency with the international VSMOW-SLAP scale (International Atomic Energy Agency, 2006), we relied on two bracketing internal standard waters: NEEM (δ^{18}O: -33.56 ± 0.05‰, δD: -257.6 ± 0.5‰) and FP5 (δ^{18}O: -50.64 ± 0.05‰, δD: -395.9 ± 0.5‰), calibrated at LSCE with mass spectrometry for δ^{18}O and with laser spectrometry for δD.

To determine the isotope-humidity relationship for calibration, vapor with known isotopic composition was generated at
105 different humidity levels, from 150 to 1500 ppmv with the low humidity level generator (in the field) and from 1000 to 5500 ppmv with the SDM (at LSCE). A well constrained relationship is determined from the 2018 data set over the whole range of humidity values (Fig. S2). We note that we do not observe differences between field and LSCE relationships. Further measurements in 2019, 2020 and 2021 show that this calibration is stable over time, as already noted by Bailey et al. (2015). This calibration curve also takes into account the shift between measured and true isotopic values. The same shift in δ^{18}O
110 and δD has been observed between measured and true value for both NEEM and FP5. We checked the mean drift of the instrument by measuring NEEM standard at 1100 ppmv using an automatic routine every 48 hours. Some technical issues led us to select only 150 calibrations over the 2-year period (Fig. S3). A large scattering was observed which was due to problem with the humidity generator during the winter and we only used the data acquired during summer field season for the drift calibration (Text S1). The estimated correction associated with the mean linear drift is insignificant with respect to
115 the humidity dependency correction and we estimate the mean uncertainty as 0.8 ‰ and 3.2 ‰ for δ^{18}O and δD respectively (details in Text S1).

2.1.2 Precipitation isotopic composition

In parallel with continuous water vapor isotopic measurements, the isotopic composition of precipitation and surface snow is also monitored. Precipitation is collected on a daily basis whenever the amount of precipitation is sufficient using a wooden
120 platform with a plastic bottom (length x width x height = 60x40x10 cm) installed at DDU station on building rooftop. Samples are sent back in -20°C shipment to LSCE once a year. Measurements are performed with a L2130-i Picarro laser spectrometer working in liquid mode. The uncertainty (1 sigma) of our data set is 0.2 ‰ and 0.7 ‰ respectively for δ^{18}O and δD. It is estimated using replicates (2 measurements) over 15 % of the samples.

2.1.3 Meteorological data

125 Meteorological data are available since 1956 at the Meteo France weather station of DDU at 3-hour resolution and 1-hour resolution. Hereafter, we use the 2-meter air temperature (°C), the specific humidity (volume mixing ratio in ppmv), calculated from pressure (mbar), temperature and relative humidity (%), as well as the wind speed (m s^{-1}) and direction (°).

2.2 ECHAM6-wiso model

ECHAM6-wiso is the isotopic version of the atmospheric general circulation model ECHAM6 (Stevens et al., 2013). The
130 implementation of the water isotopes in ECHAM6 has been described in detail by Cauquoin et al. (2019), and has been

updated in several aspects by Cauquoin and Werner (2021) to make the model results more consistent with the last findings based on water isotope observations (isotopic composition of snow on sea ice taken into account, supersaturation equation slightly updated, and kinetic fractionation factors for oceanic evaporation assumed to be independent of wind speed). We have used ECHAM6-wiso model outputs from a simulation at high spatial resolution (at T127L95, 0.9° horizontal resolution and 95 vertical levels) nudged to ERA5 reanalysis (Hersbach et al., 2020). The ECHAM6-wiso 3D-fields of temperature, vorticity and divergence as well as the surface pressure field were nudged toward the ERA5 reanalysis data every 6 hours. The orbital parameters and greenhouse gases concentrations have been set to the values of the corresponding model year. The monthly mean sea surface temperature (SST) and sea-ice fields from the ERA5 reanalysis have been applied as ocean surface boundary conditions, as well as a mean $\delta^{18}O$ of surface seawater reconstruction from the global gridded data set of LeGrande and Schmidt (2006). As no equivalent data set of the δD composition of seawater exists, the deuterium isotopic composition of the seawater in any grid cell has been set equal to the related $\delta^{18}O$ composition, multiplied by a factor of 8, in accordance with the observed relation for meteoric water on a global scale (Craig, 1961). The ECHAM6-wiso simulation is described in detail and evaluated in Cauquoin and Werner (2021).

3 Results

3.1 Vapor and precipitation records

We present the full 2019-2020 record of hourly atmospheric vapor isotopic composition at DDU (Fig. 2). The mean temperature and humidity over the two-year measurement period (-11.2 °C and 1883 ppmv) are close to the average value calculated over the full dataset available from Meteo France since 1957 (-10.8 °C and 1826 ppmv), and show similar seasonal cycles (Fig. 2). A clear seasonal cycle is observed for all variables except d-excess (Tab. 1), with higher mean values in summer (-2.3 °C, 3354 ppmv and -27.5 ‰ for temperature, humidity and $\delta^{18}O$ respectively in December, January and February (DJF)) than in winter (-17.0 °C, 1185 ppmv, -34.8 ‰ in June, July and August (JJA)). The difference of d-excess mean value between winter and summer (2.4 ‰) is not significant compared to the standard deviation (3.2 and 3.3 ‰ for DJF and JJA, respectively).

The variability of temperature, $\delta^{18}O$ and humidity also shows a seasonality (Tab. 1), with higher standard deviation in winter than in summer. These results can be explained by a different seasonal impact of the main precipitation events. Blue bars in Figure 2 show the distribution of the 3-day periods centered on daily precipitation rates higher than 4.5 $\mathrm{kg\,m^{-2}\,day^{-1}}$. We detect 35 precipitation peaks over the 2-year period, 7 (20 %) during DJF (summer) and 8 (23 %) during JJA (winter), so no seasonality of the occurrence is observed. Though, the temperature anomalies associated with those events are more important in winter (Fig. S4). Servettaz et al. (2020) demonstrated the key role that such precipitation events, controlled by synoptic scale dynamics, could play in ice-core interpretation at high accumulation sites. As they are associated with warm and moist air intrusions, they cause warm anomalies compared to the seasonal mean. Here, we point out two major events that are particularly intense during extended winter (from May to September): (a) 23 July 2019, with a precipitation rate of 31 $\mathrm{kg\,m^{-2}\,day^{-1}}$ and (b) 2 July 2020, with a precipitation rate of 21 $\mathrm{kg\,m^{-2}\,day^{-1}}$. These events correspond to the largest daily precipitation rates of each winter, and to the first and third largest daily precipitation rates when considering the whole
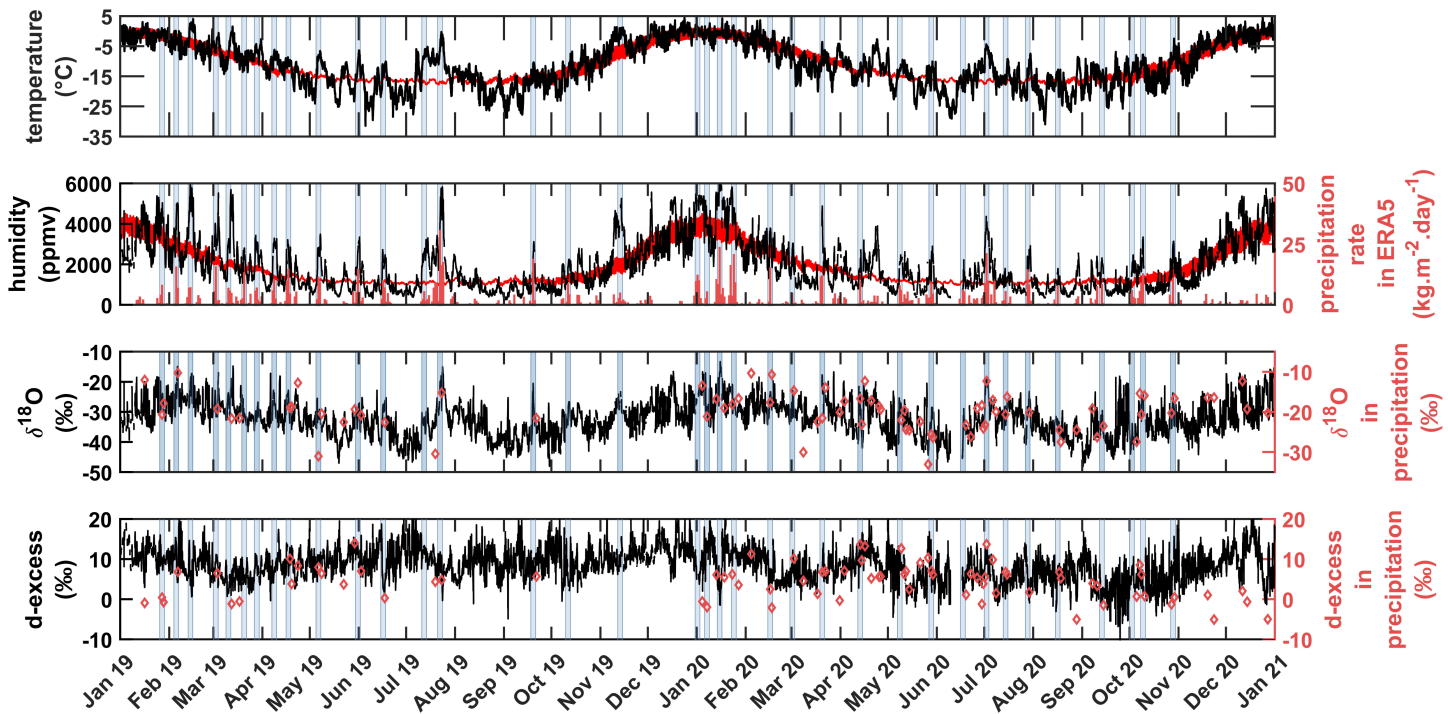
Figure 2. Two-year data series (1 Jan. 2019 to 31 Dec. 2020) of meteorological and isotopic measurements at DDU. Panels from top to bottom: 1) hourly 2m-temperature (°C) from Meteo France weather station in black, 3-hour temperature averaged over 1957-2020 period in red. 2) hourly humidity (ppmv) measured by the Picarro laser spectrometer in black, mean humidity (ppmv) from Meteo France weather station averaged over the 1957-2020 period in red; red bars indicate daily precipitation rate from ERA5 reanalysis (in $\mathrm{kg\,m^{-2}\,day^{-1}}$). 3) calibrated $\delta^{18}\mathrm{O}$ (‰) in water vapor (hourly average in black) and in precipitation (red diamonds). 4) d-excess (‰) in water vapor (hourly average in black) and in precipitation (red diamonds). Light blue bars indicate the 3-day periods centered on high daily precipitation rates (peaks) with value higher than $4.5\ \mathrm{kg\,m^{-2}\,day^{-1}}$ and separated by a minimum of 5 days.

2019-2020 period. The values of temperature, humidity and $\delta^{18}\mathrm{O}$ during these winter events (-1 °C and -4.4 °C, 5780 ppmv
165 and 4370 ppmv, -17.8 ‰ and -19.3 ‰, respectively for the two events) are close or above summer averages (Tab. 1).

As mentioned above, synoptic events are not clearly visible in summer. Summer variability is actually dominated by the succession of diurnal cycles. In Figure 3, we show the mean diurnal cycles in summer and winter. During winter, the diurnal cycles of temperature and humidity are flattened to 0.6 °C and 40 ppmv, and are not visible for $\delta^{18}\mathrm{O}$ and d-excess (Fig. 3). The summer diurnal cycle amplitudes reach almost 4°C, 1000 ppmv and 4 ‰ for temperature, humidity and $\delta^{18}\mathrm{O}$, respectively.
170 The d-excess summer diurnal cycle amplitude (about 1 ‰) is smaller than the uncertainty and therefore hardly significant. The summer amplitudes of temperature and humidity diurnal cycles over the 2019-2020 study period are similar to the diurnal variability in temperature and humidity over the whole instrumental period (1957-2020). This summer diurnal cycle has been documented in previous detailed studies (Pettré et al., 1993; Bréant et al., 2019) and attributed to katabatic wind variability

Table 1. Mean and standard deviation (std) of temperature (temp.), humidity (hum.) and isotopic composition of water vapor calculated from daily means (left). Correlations are calculated with daily data (right). The period considered is 2019-2020 except for "historical" (hist.) data which are the mean of daily averages over 1957-2020.

	Temp. (°C)		Hum. (ppmv)			$\delta^{18}O$ (‰)		d-excess (‰)		$\delta^{18}O$ vs Hum		$\delta^{18}O$ vs Temp.	
	mean	std	mean	std	relative std (%)	mean	std	mean	std	slope (‰ $ppmv^{-1}$)	R^2	slope (‰ $°C^{-1}$)	R^2
DJF	-2.3	2.4	3373	998	30	-27.4	3.5	10.2	3.2	$2.4\ 10^{-3}$	0.45	//	0.06
JJA	-16.9	5.0	1194	783	66	-34.7	5.0	7.8	3.3	$4.5\ 10^{-3}$	0.51	0.64	0.42
Total	-11.2	7.1	1833	1196	65	-32.3	5.2	8.4	3.4	$3.4\ 10^{-3}$	0.61	0.52	0.51
Hist.	-10.8	5.9	1826	902	49	//	//	//	//	//	//	//	//

particularly during clear sky conditions, when the sun zenithal angle impacts the radiative cooling of the continental surface responsible for the katabatic flow. When the sun is at its lowest position, cold and dry air masses coming from inland are associated with low $\delta^{18}O$ values. On the contrary, when the sun is at its highest position, the origin of humid air masses is more local, through convective mixing for instance, and we observe a parallel increase in humidity, temperature and $\delta^{18}O$.

Differences between winter and summer weather regimes impact the relationship between variables in vapor. First, humidity and $\delta^{18}O$ show high correlation coefficients (calculated from daily means) both over the whole record (R^2=0.6) and at a seasonal scale (R^2=0.5 for DJF and JJA). The slope of this linear relationship (Tab. 1 and Fig. S5) is almost doubled during winter ($4.5.10^{-3}$ ‰ $ppmv^{-1}$) compared to summer ($2.4.10^{-3}$ ‰ $ppmv^{-1}$). This difference between low and high humidity regimes (during winter and summer, respectively) is expected from the relationships between $\delta^{18}O$ and humidity along distillation line or during mixing of 2 different air masses (Steen-Larsen et al., 2017). Second, the linear relationship between $\delta^{18}O$ and temperature is strong for the full period (R^2=0.5) but vanishes during summer (R^2<0.1). This can be related to the smaller daily variability during summer, in comparison to winter when synoptic event occurrences lead to larger increase of temperature and $\delta^{18}O$ over synoptic time scale. The $\delta^{18}O$-temperature slope (Tab. 1 and Fig. S6) over the full period (0.5 ‰ $°C^{-1}$) is similar to the winter mean slope (0.6 ‰ $°C^{-1}$, R^2=0.4). We note that spring mean slope is slightly different (0.4 ‰ $°C^{-1}$, R^2=0.3) but is statistically less representative in comparison. Further, we need to investigate the link between the isotopic composition of vapor and precipitation to study the impact on ice-core interpretation. The condensation of vapor in the upper atmospheric layers leads to precipitation but subsequent exchanges between atmospheric water vapor and snow flakes can also affect the isotopic composition of the collected precipitation. Classically a unique slope (site dependent) is used to convert isotopic signal into temperature.

Over the 2019-2020 period, we collected 82 precipitation samples (Fig. 2). In order to compare isotopic signals in precipitation and vapor, we calculate the theoretical isotopic composition of vapor at equilibrium with each precipitation sample. We use solid-vapor fractionation coefficients at equilibrium from Majoube (1971) and Merlivat and Nief (1967) calculated with the daily 2m-temperature corresponding to the day of sample collection. The comparison is made with the daily averaged isotopic
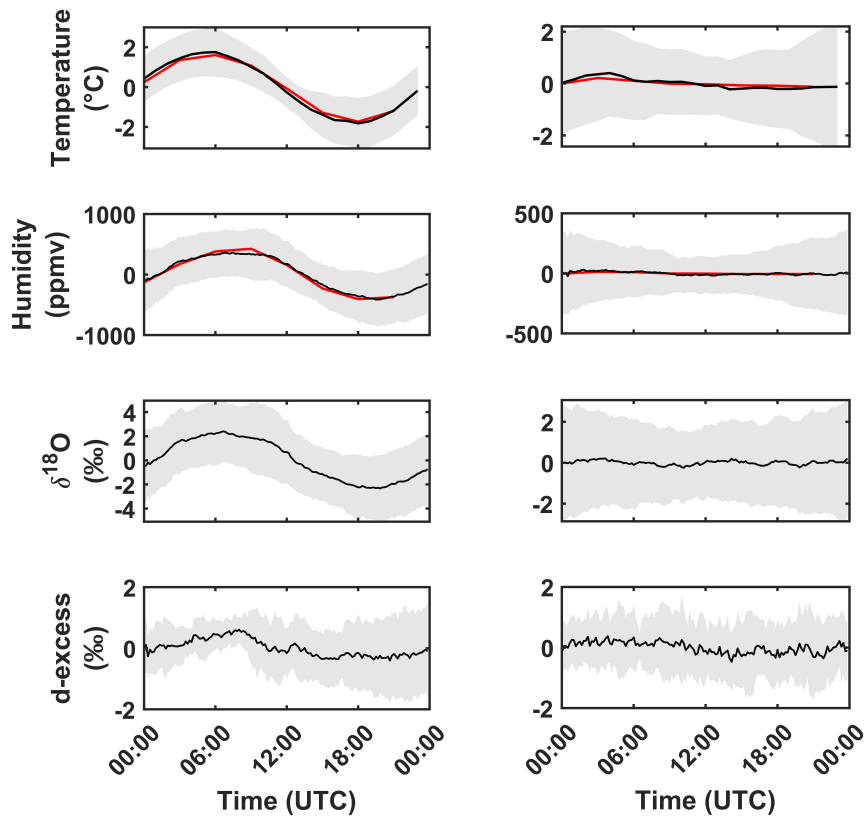
Figure 3. Mean diurnal cycles estimated from hourly data in summer (DJF, left panel) and winter (JJA, right panel) over the 2019-2020 period. Red lines are computed from the historical Meteo France weather station data set (1957-2020 period, 3-hour resolution). DDU time is UTC+10.

composition of water vapor measured at DDU (Fig. S7). Results exhibit a clear linear relationship between both datasets ($R^2 =$ 0.5) with a slope of $0.7\,\%_o\,\%_o^{-1}$. Note that we do not expect a correlation coefficient and slope of 1 because we averaged over 24h while the precipitation event is often shorter and precipitation samples can be affected by post-deposition effects before their collection. Furthermore the daily precipitation δ^{18}O samples are strongly scattered and it is not possible to observe in the precipitation δ^{18}O record an equivalent to the strong peaks observed in the water vapor δ^{18}O during the two strong mid-winter synoptic events. Because the sampling of precipitation was limited to one sample per day and only for the days with precipitation, it is expected that we cannot observe the same δ^{18}O signal in the precipitation record than in the continuous water vapor at an hourly resolution.
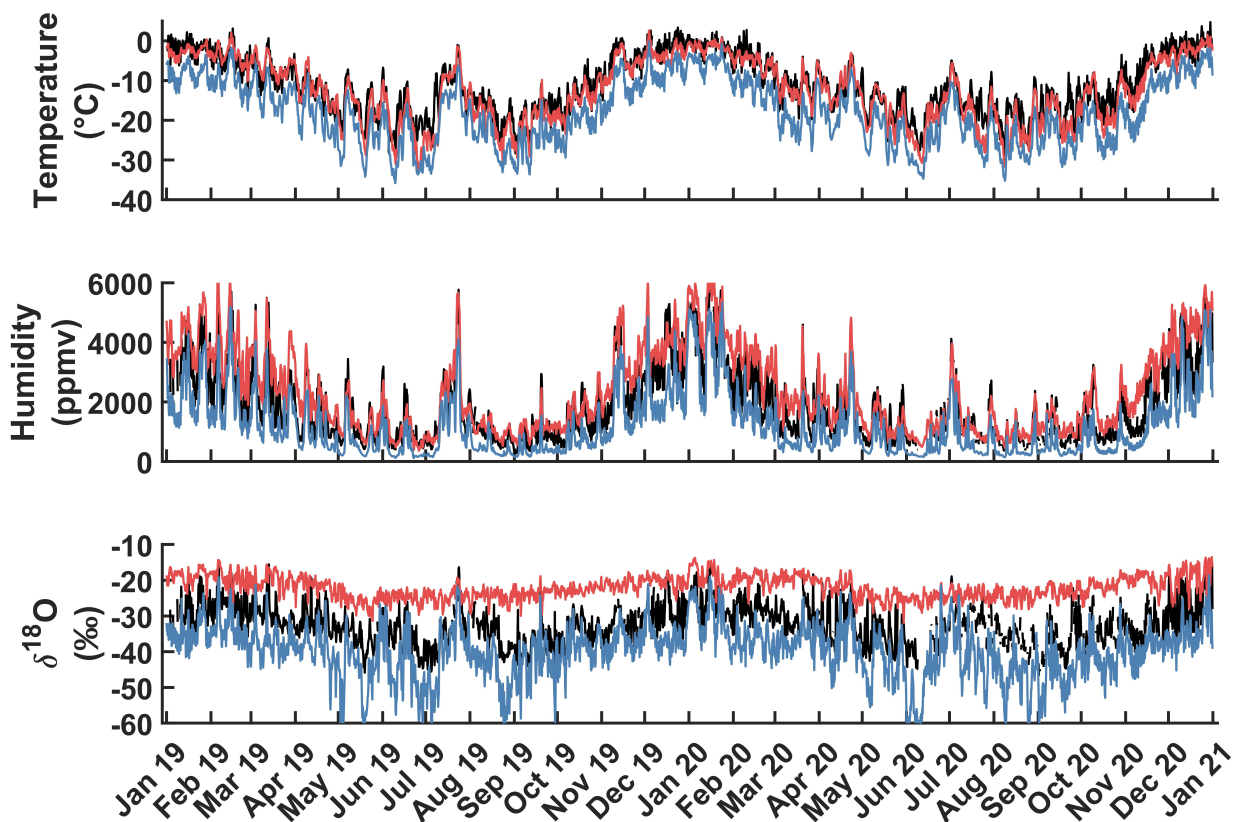
9

Figure 4. Meteorological and isotopic measurements at DDU at 6-hourly resolution, in black. Panels from top to bottom: 1) 2m-temperature ($^{\circ}$C) from Meteo France weather station, 2) humidity (ppmv) measured by the Picarro laser spectrometer; 3) δ^{18}O (‰) in water vapor. Colored lines are ECHAM6-wiso first level outputs (6-hourly resolution): the red (blue) line is representing the mean of oceanic (continental) grid cells.

3.2 ECHAM6-wiso: data-model comparison at DDU

205

To compare ECHAM6-wiso outputs and DDU measurements of temperature, humidity and δ^{18}O, we consider the four ECHAM6-wiso grid cells around DDU station (Fig. 1). Since isotopic variables are not available at 2 m above the ground in ECHAM6-wiso, we consider all modeled variables at the lowest atmospheric level in ECHAM6-wiso (approximately 75 m above the ground, see exact altitudes in Tab. S1) in order to work with an homogeneous data set. We have combined oceanic (continen-

210 tal) cells using the average values of grid cells outputs #1 and #3 (#2 and #4) to plot Figure 4. Indeed, both oceanic (continental) cells show very similar characteristics (i.e. mean values, standard deviation, correlations with DDU measurements; Fig. S8 and Tab. S1).

Modeled temperature always present a cold bias (-1.2 °C for the oceanic grid cell and -6.7 °C for the continental grid cell) compared to measurements at DDU, while humidity bias is either positive (about 500 ppmv in average for oceanic grid cells) or negative (about -600 ppmv in average for continental grid cells). The temperature bias is not related to the average mean altitude of grid cells, as a similar comparison using the modeled 2m-temperature also results in cold biases (Tab. S1). We observe a bias of -3 °C in ERA5 2m-temperature in comparison to measurements over the 2 years data set which could explain the differences in temperature between model and measurements as suggested by Goursaud et al. (2018). Despite these biases, ECHAM6-wiso outputs reproduce well the variability of the temperature and humidity records at DDU for both oceanic and continental grid cells. Over the full period, modeled daily temperature and humidity are highly correlated to observations (R^2 = 0.9, Tab. S1) and both show very similar standard deviations (about 8 °C and 1200 ppmv for both continental and oceanic cells for temperature and humidity respectively, compared to 7 °C and 1200 ppmv for observations, Tab. 1 and Tab. S1).

However the modeled water vapor $\delta^{18}O$ signals for oceanic and continental grid cells are very different and neither of them fits the measurements. In particular, the variability of the simulated water vapor $\delta^{18}O$ in the oceanic grid cell (std of 2.9 ‰) is lower than in the DDU record (std of 5.2 ‰), while the variability in the continental grid cell is higher (7.1 ‰). Finally, the correlation between data and modeled water vapor $\delta^{18}O$ is better for the continental grid cell (R^2=0.5) than for the oceanic grid cell (R^2=0.3). These results show that the modeled water vapor isotopic composition in this region at the frontier between the Antarctic ice sheet and ocean areas is strongly sensitive to the cell position over the ocean or the continent, more than for variables like temperature or humidity. It follows that both oceanic and continental influences must be considered to interpret our isotopic signal at DDU.

In the following we combine both oceanic and continental grid cells to build a modeled time series of temperature, humidity and water vapor $\delta^{18}O$ comparable with our observations. For temperature and humidity, we directly compute weighted averages of the two grid cells time series, while for $\delta^{18}O$ we also take into account the humidity content of each air mass to compute the combined weighted isotopic ratio. Three weighing approaches are investigated: a) weights based on the distance between DDU coordinates and grid cell centers, b) weights computed to minimize the distance between measured and modeled mean humidity (Nelder-Mead simplex algorithm as described in Lagarias et al. (1998)) and c) weights computed as in b) but with $\delta^{18}O$ as target. If we look at the mean isotopic compositions and standard deviations of model data sets and the correlation coefficients (combination data sets vs. observations) we observe that the three sets of weights improve the comparison between ECHAM6-wiso $\delta^{18}O$ outputs and measurements at DDU compared to individual grid cells (Tab. 2 and Tab. S1).

In Figure 5 we present the results obtained with the weighing scheme c, targeting the best agreement for $\delta^{18}O$ and leading to the highest correlations coefficients between measurements and model outputs for temperature (R^2=0.9), humidity (R^2=0.9) and $\delta^{18}O$ (R^2=0.6), slopes close to 1 for linear regression between observation and model outputs (1.1, 0.9 and 0.6 for temperature, humidity and $\delta^{18}O$ respectively), and the lowest difference between observed and modeled $\delta^{18}O$ standard deviation (0.8 ‰). We notice an expected cold bias (probably due to ERA5 cold bias at DDU, see previous paragraph) and a dry bias probably due to an altitude effect (continental grid cell mean altitude is 673 m.a.sl.). This configuration corresponds to a combination of 79% of continental air masses and 21% of oceanic air masses, which gives less weight to the ocean grid cells than the other two combinations (Tab. 2). This shows that only a strong continental influence can explain the isotopic signal recorded

Table 2. ECHAM6-wiso combination (a, b and c, see Text) of first level outputs results and comparison with measurements. Mean and standard deviation of meteorological variables and isotopic composition (left section). Correlations between model and observations (middle section). Weights of each grid cell for the different computation schemes (right section).

Criteria	Temperature		Humidity		$\delta^{18}O$		Temp. corr. (ECHAM vs Meas.)		Hum corr. (ECHAM vs Meas.)		$\delta^{18}O$ corr. (ECHAM vs Meas.)		Oceanic (70 m a.s.l.)	Continental (673 m a.s.l.)
	mean	std	mean	std	mean	std	slope	R^2	slope	R^2	slope	R^2	weight	weight
a: distance	-16.2	7.9	1566	1135	-30.7	3.9	1.1	0.9	0.9	0.9	0.5	0.5	0.31	0.69
b: humidity	-15.1	7.9	1800	1203	-26.9	3.3	1.1	0.9	1.0	0.9	0.4	0.4	0.48	0.52
c: isotope	-16.7	8.0	1458	1107	-32.5	4.4	1.1	0.9	0.9	0.9	0.6	0.6	0.21	0.79
Measurements	-11.2	7.1	1833	1196	-32.3	5.2								

Table 3. Mean and standard deviation (std) of meteorological variables and isotopic composition calculated from daily means (left). Correlations are calculated with daily data (right). Top: from DDU measurements. Bottom: from ECHAM6-wiso first level outputs using the c configuration (Tab.2) of cell combinations.

		Temperature (°C)		Hum. (ppmv)			$\delta^{18}O$ (‰)		d-excess (‰)		$\delta^{18}O$ vs hum.		$\delta^{18}O$ vs temp.	
		mean	std	mean	std	relative std (%)	mean	std	mean	std	slope (‰ ppmv^{-1})	R^2	slope (‰ °C^{-1})	R^2
DDU	DJF	-2.3	2.4	3373	998	30	-27.4	3.5	10.2	3.2	$2.4\ 10^{-3}$	0.45	//	0.06
	JJA	-16.9	5.0	1194	783	66	-34.7	5.0	7.8	3.3	$4.5\ 10^{-3}$	0.51	0.64	0.42
	Total	-11.2	7.1	1833	1196	65	-32.3	5.2	8.4	3.4	$3.4\ 10^{-3}$	0.61	0.52	0.51
ECHAM	DJF	-7.1	2.8	2815	1002	38	-29.1	3.2	6.5	3.1	$1.9\ 10^{-3}$	0.4	//	0.1
	JJA	-23.1	6.2	783	664	88	-35.7	4.4	9.3	4.8	$4.2\ 10^{-3}$	0.4	0.47	0.4
	Total	-16.7	8.0	1458	1107	79	-32.5	4.4	7.8	4.4	$2.6\ 10^{-3}$	0.4	0.38	0.5

at DDU. At the seasonal scale, the modeled time series issued from configuration c shows similar characteristics (average value, variability) to observations for humidity, temperature and water vapor isotopic composition (Tab. 3). As for d-excess, while modeled average value (7.8‰) and variability (4.4‰) are close to measured ones (Fig. S9), model fails to reproduce the seasonality of observation. Seasonality is actually inverted in the model: while d-excess reached its maximum in summer (DJF) in observations (10.2‰), its value is minimal in ECHAM6-wiso combination (6.5‰). We will thus only consider the $\delta^{18}O$ in the following.

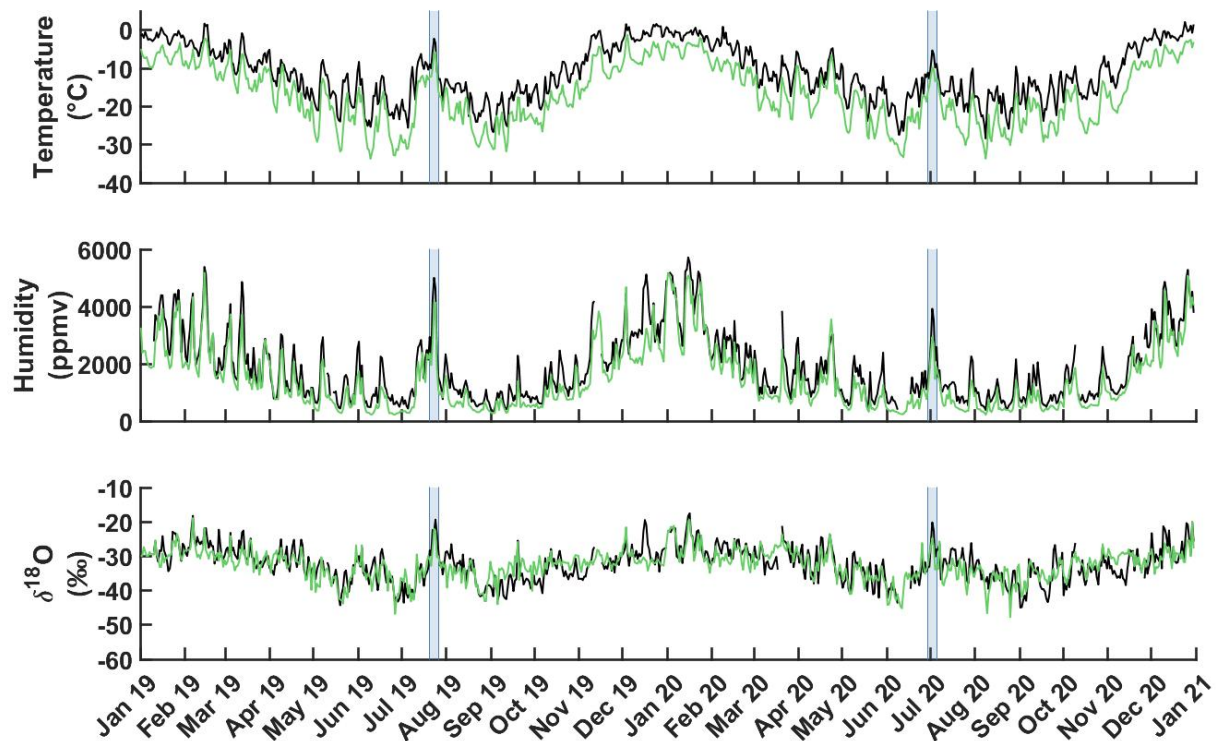**Figure 5.** Comparison of temperature, humidity and δ^{18}O modeled by ECHAM6-wiso and measured at DDU station over the period 2019-2020. Meteorological and isotopic measurements at DDU at daily resolution are shown in black. Panels from top to bottom: 1) 2m-temperature ($^{\circ}$C) from Meteo France weather station, 2) humidity (ppmv) measured by the Picarro laser spectrometer; 3) water vapor δ^{18}O (‰). Green lines correspond to the ECHAM6-wiso combination of surface air level outputs (daily resolution) using configuration c (see text). Light blue bars indicate major winter synoptics events of 23 July 2019 and 2 July 2020 (see text).

We focus on the two major winter synoptics events of 23 July 2019 and 2 July 2020 identified in the previous section. Those 255 winter events are associated with peaks in meteorological variables and isotopic values (temperature, humidity and δ^{18}O) close or even higher than summer means in the observations (section 3.1) as well as in the model outputs (-5.9°C and -9.9°C, 4130 ppmv and 2930 ppmv, -22.1 ‰ and -24.8 ‰, respectively for the two events) (Fig. 5 and Tab. 3). The amplitudes of these peaks in ECHAM6-wiso are comparable to that of measurements. This confirms that ECHAM6-wiso is able to reproduce the variability of the meteorological and isotopic signals even during extreme events.

260 Finally, we compare ECHAM6-wiso daily means of precipitation isotopic composition with observations. We obtain a weak but still significant correlation coefficient between both data sets (R^2=0.3) and the slope of the linear regression is 0.4 ‰ ‰$^{-1}$ (Fig. S10). In particular, the seasonal cycle is well captured both by the observations and the model outputs with lower mean

δ^{18}O values during winter and higher mean δ^{18}O during summer (Fig. S11). In addition, we observe that the relationship between isotopic composition of vapor and precipitation is mainly preserved in ECHAM6-wiso (Fig. S12).

265   The above comparisons between model and observation support the use of ECHAM6-wiso to interpret the isotopic signal variability in water vapor and precipitation at the seasonal and interannual scale in the surrounding of the DDU station. It is thus a very powerful tool to help interpreting snow and ice cores in the region.

4   Discussion

The water isotopic series shown above have highlighted the complex relationships between temperature and δ^{18}O of vapor and
270   precipitation at DDU. We have also shown that the atmospheric model equipped with water isotope ECHAM6-wiso reproduces daily and seasonal mean and variability of the isotopic observation records. In the following, we explore how this model can help interpreting firn cores isotopic records in Adelie Land. For this, we us the S1C1 firn core analyzed by Goursaud et al. (2017). This 22.4 m core has been drilled during the 2006/2007 season at 66.71°S, 139.8°E, 279 m a.s.l., 15 km from DDU (Fig. 1). It covers 60 years with a mean accumulation rate of $218 \pm 69 \, \mathrm{kg \, m^{-2} \, yr^{-1}}$ but we will limit our study to the period
275   back to 1979 in order to be able to compare with reanalyses data. The S1C1 δ^{18}O record measured with a resolution of 5 cm (Fig. 6a) shows variations with a maximum amplitude of δ^{18}O variations of 10 ‰. There is no clear annual periodicity in the δ^{18}O as seen in the frequency spectrum (Fig. 6b).

We create virtual firn cores (VFC) following the approach of Sime et al. (2011) to study the origin of the δ^{18}O variations in the S1C1 core (Text S2). The first VFC is obtained using temperature and precipitation from ERA5 (red curves in Fig. 6): δ^{18}O
280   is directly linked to temperature weighted by precipitation to account for precipitation intermittency. For this construction, we used the slope of 0.44 ‰ °C^{-1} observed at DDU between δ^{18}O of precipitation and temperature (Fig. S13). This first VFC, hereafter called VFC-ERA5, displays clear annual cycles of δ^{18}O with an average amplitude of 7‰ (Fig. 6a). The standard deviation of the signal remains stable over time which is different from the S1C1 δ^{18}O record showing large variations of the standard deviation with depth (Fig. S14a). The frequency spectrum indeed reveals a marked annual periodicity (Fig. 6b).

285   The poor agreement between VFC-ERA5 and S1C1 δ^{18}O records (Fig. 6a and 6b) clearly confirms that temperature is not the only driver of δ^{18}O in this Adelie Land firn core. We have also produced a second VFC based on the outputs of ECHAM6-wiso (green curves in Fig. 6). In this case, the δ^{18}O record of VFC-ECHAM is calculated from the δ^{18}O of precipitation and precipitation amount, both simulated by ECHAM6-wiso back to 1979 and provided at a 6-hourly resolution. As for the VFC-ERA5, the VFC-ECHAM record displays a clear annual cycle visible in the associated spectrum (Fig. 6b). However, it
290   displays a much larger variability in the amplitude of the annual cycle than the VFC-ERA5. This results in larger variations of the moving standard deviation of VFC-ECHAM δ^{18}O record which looks like variations observed in the temporal evolution of the standard deviation of S1C1 δ^{18}O record (Fig. S14a). There is thus, in general, a better agreement of S1C1 δ^{18}O record with VFC-ECHAM δ^{18}O record than with VFC-ERA5 δ^{18}O record. Still, the amplitude of the standard deviation of VFC-ECHAM δ^{18}O record doesn't show the same clear decreasing trend as observed in S1C1 record, a difference which may be attributed to
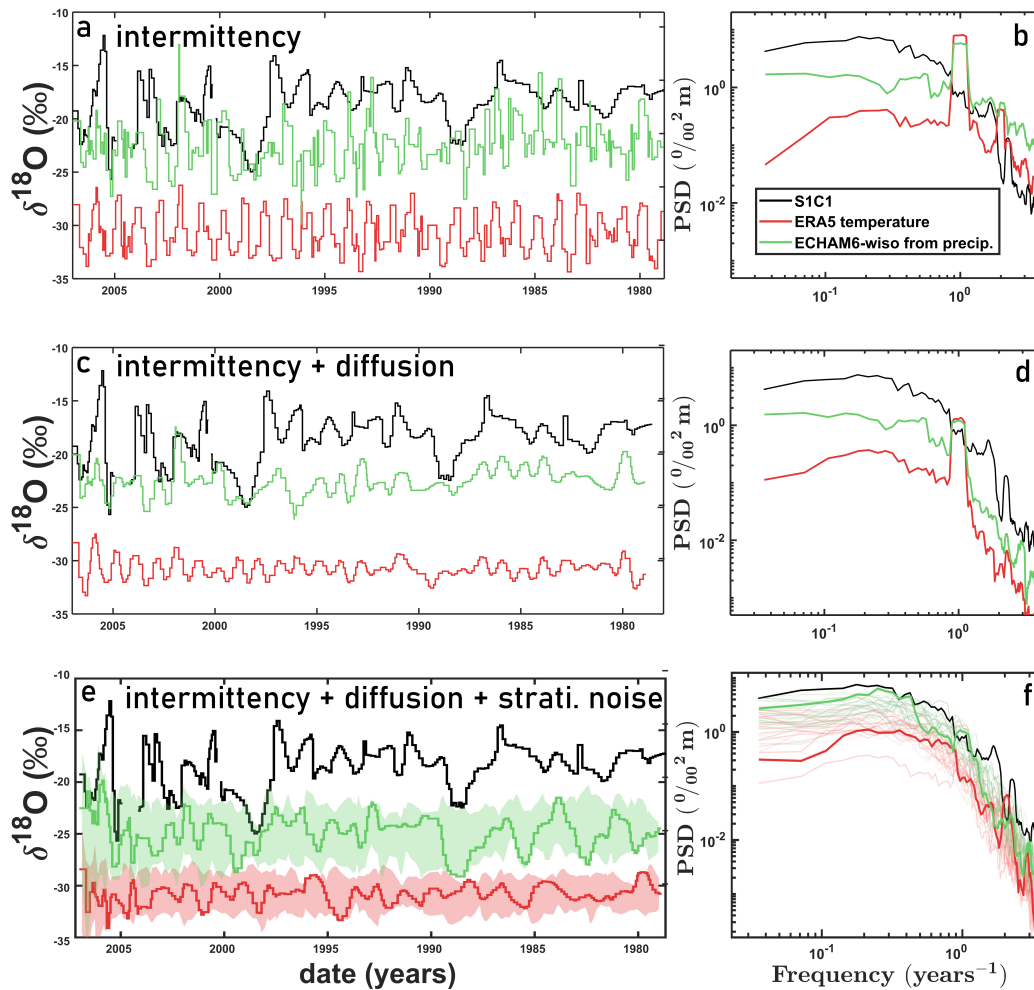295   the diffusion of water isotopes within the firn.

14

Figure 6. In black, isotopic composition (δ^{18}O in ‰) of S1C1 (first 620 cm of water equivalent) firn core versus date (years) using the dating based on chemical analyses in Goursaud et al. (2017). Red and green curves are the isotopic compositions of VFC resampled at S1C1 sampling resolution and based on temperature from ERA5 and on ECHAM6-wiso isotopic composition of precipitation, respectively (see text). In the first row, a) and b) VFCs are calculated with precipitation intermittency. In the second row, c) and d) VFCs are built with precipitation intermittency and isotopic diffusion. In the third row, e) and f) VFCs are calculated with precipitation intermittency, isotopic diffusion and simulated stratigraphic noise (25 random noise simulation). In panels a,c,f, an artificial bias is added to VFCs (-5‰ and -10‰, respectively for green and red curves) in order to improve readability. Right column presents the associated frequency spectrums computed using Thomson's multitaper power spectral density. One stratigraphic noise simulation is highlighted in bold as an example, other simulations are represented by shaded envelop (e) or light plots (f).

In Figure 6c, the influence of isotopic diffusion in the firn has been considered for the construction of the VFC records (details in Text S3). The rapid decrease of the amplitude of the annual cycles with increasing depth in S1C1 is reproduced by

this VFC. This effect is also seen in the associated spectrum (Fig. 6d) with a decrease of the power in the high frequency range (from 1.2 to 0.04 $\%o^2$ m in average for frequencies greater than 1.1 yr^{-1}, in VFC-ECHAM), below the level of S1C1 spectrum.

Diffusion also induces strong decrease of the standard deviation amplitude of the standard deviations of the VFC-ERA5 and VFC-ECHAM records (Fig. S14, Tab. S2), again below the level observed in the S1C1 record. This may be due to a too strong diffusion effect in our approach. Improvement of the diffusion model may be able to reconcile the amplitude of the high frequency variability of the VFC δ^{18}O signals with the amplitude of the high frequency variability of the S1C1 δ^{18}O signal. It may however not explain why there is no clear temporal correspondence between S1C1 δ^{18}O signal and the VFC δ^{18}O signal, nor why the annual cycle is not seen in the S1C1 signal, which may be explained by errors in the chronology of the S1C1 core. Another point of disagreement is the lower power associated with low frequency signal in the VFC records than in the S1C1 signal. These three points of disagreement may be caused by deposition or post-deposition effects creating a non climatic low frequency variability while destroying the record of the annual variability (through wind blowing for example). To simulate such an effect, we follow Laepple et al. (2018) by adding white stratigraphic noise that is controlled by two parameters: (i) the relative amount of noise compared to the input signal (0 % to 100 %) and (ii) the length at which the noise impacts the signal (from 1 to 10 cm). In Figure 6e, we show that using a noise level of 90 % and a noise scale of 7 cm, the VFC-ECHAM inter-annual amplitude variability is more likely to match S1C1 signal. This is confirmed by spectral analyses (Fig. 6f), in wich the difference between S1C1 and VFC-ECHAM spectrums become comparable (4.1 and 2.3 $\%o^2$ m in average for low frequencies i.e. from 0.1 to 0.5 $years^{-1}$, respectively for S1C1 and ECHAM, for example). We also notice that even with a noise level of 100 % (maximum authorized in this model), the ERA5-VFC spectrums hardly improve in comparison with observation (0.9 $\%o^2$ m in average for low frequencies, for example). Note that invoking a strong stratigraphic noise level to explain the difference in the spectrum obtained for S1C1 and the VFC cores is not the only explanation. The linear relationship estimated between δ^{18}O of vapor and precipitation at DDU shows that precipitation only imprints part of the vapor signal variability (slope = 0.6 $\%o\%o^{-1}$ with R^2=0.4 in ECHAM6-wiso, see Fig. S12). A too low interannual climatic variability in the δ^{18}O of model precipitation would also explain the lower power in the low frequency range of the spectrums of the VFC records.

As a conclusion, we have shown that using of ECHAM6-wiso outputs better explain the firn core δ^{18}O variability than considering only the temperature influence. Still, the interannual δ^{18}O variability simulated by ECHAM6-wiso is not able to explain the low frequency variability of the firn core δ^{18}O in Adelie Land. This could be explained by stratigraphic noise associate with deposition and post-deposition effects, and maybe an underestimation of the interannual variability of precipitation and their isotopic signal in the model. In order to cancel the influence of stratigraphic noise and increase the signal to noise ratio, we would need to stack several firn core (Münch and Laepple, 2018; Laepple et al., 2016, 2018; Casado et al., 2020).

5   Conclusions

We present the first multi-year continuous record of isotopic composition in surface vapor and precipitation at Dumont d'Urville station (Adélie Land), a coastal site in East Antarctica. This region is characterized by the presence of strong katabatic winds and the local influence of ocean and sea ice. This new dataset allows us to characterize diurnal variations of meteorological

variables (temperature, humidity and δ^{18}O) for the different seasons and to determine the evolution of key relationships (δ^{18}O versus temperature or humidity) along the year. We found mean annual slopes of 0.5 and 0.4 ‰ °C^{-1} for daily δ^{18}O vs. temperature in the water vapor and in the precipitation respectively (with R^2=0.5 and 0.2) . The warm and wet synoptic events occurring in winter and associated with strong precipitation are clearly imprinted in the water vapor isotopic signal while our snow samplings mainly capture the strong seasonal cycle. We evaluate the ECHAM6-wiso model through a comparison of the simulated δ^{18}O of water vapor and precipitation with our record and we show that a combination of continental (79 %) and oceanic (21 %) grid cells leads the modeled temperature, humidity and δ^{18}O to nicely fit trends and variability of observations. Winter extreme synoptic events are also correctly represented by the model. The excellent agreement between modeled and measured isotopic series encourages us to investigate how ECHAM6-wiso could help understanding isotopic signals recorded in firn-cores in the region. We focus on the S1C1 firn core previously studied and located 10 km inland from DDU. Constructing virtual firn cores from modeled temperature or from water isotope and taking into account the precipitation intermittency, we show that a pure temperature interpretation fails in explaining the interannual variability observed in the measured S1C1 isotopic record. We improve the agreement between measured and modeled records when using the water isotopic composition of precipitation instead of temperature, but the low frequency variability is still underestimated. Our results suggest that both deposition and post-deposition effects contribute significantly to the isotopic signal recorded in S1C1 core. Precipitation in ECHAM6-wiso model may also underestimate variability at interannual to decadal scales in Adelie Land. Stacking several firn core records in the region to get rid of the stratigraphical noise could help disentangling these two effects.

Supplement. The supplement related to this article is available on-line at: DOI/XXX

Author contributions. CLDS analyzed data, produced plots, designed and wrote all sections of the original paper, with input from coauthors revising the text. EL and AL made substantial contribution with substantial contributions throughout the paper text. CA made substantial

17

contribution to sections 3.2 with data analysis. AL made substantial contribution to sections 3.1 and 4. MC contributed to section 4 through VFC script and outputs interpretation. AC and MW contributed with ECHAM6-wiso data analysis. BM and FP analyzed snow samples. OJ is responsible for remote control of the setup at DDU. LP made plot S11. All authors provided comments to the manuscript.

References

Altnau, S., Schlosser, E., Isaksson, E., and Divine, D.: Climatic signals from 76 shallow firn cores in Dronning Maud Land, East Antarctica, The Cryosphere, 9, 925–944, https://doi.org/10.5194/tc-9-925-2015, 2015.

Bagheri Dastgerdi, S., Behrens, M., Bonne, J.-L., Hörhold, M., Lohmann, G., Schlosser, E., and Werner, M.: Continuous monitoring of surface water vapour isotopic compositions at Neumayer Station III, East Antarctica, The Cryosphere Discuss., 2020, 1–34, https://doi.org/10.5194/tc-2020-302, publisher: Copernicus Publications, 2020.

Bailey, A., Noone, D., Berkelhammer, M., Steen-Larsen, H. C., and Sato, P.: The stability and calibration of water vapor isotope ratio measurements during long-term deployments, Atmospheric Measurement Techniques, 8, 4521–4538, https://doi.org/10.5194/amt-8-4521-2015, 2015.

Bonne, J.-L., Masson-Delmotte, V., Cattani, O., Delmotte, M., Risi, C., Sodemann, H., and Steen-Larsen, H. C.: The isotopic composition of water vapour and precipitation in Ivittuut, southern Greenland, Atmospheric Chemistry and Physics, 14, 4419–4439, https://doi.org/10.5194/acp-14-4419-2014, 2014.

Bréant, C., Leroy-Dos Santos, C., Agosta, C., Casado, M., Fourré, E., Goursaud, S., Masson-Delmotte, V., Favier, V., Cattani, O., Prié, F., Golly, B., Orsi, A., Martinerie, P., and Landais, A.: Coastal water vapor isotopic composition driven by katabatic wind variability in summer at Dumont d'Urville, coastal East Antarctica, Earth and Planetary Science Letters, 514, 37–47, https://doi.org/10.1016/j.epsl.2019.03.004, 2019.

Casado, M., Landais, A., Masson-Delmotte, V., Genthon, C., Kerstel, E., Kassi, S., Arnaud, L., Picard, G., Prie, F., Cattani, O., Steen-Larsen, H.-C., Vignon, E., and Cermak, P.: Continuous measurements of isotopic composition of water vapour on the EastAntarctic Plateau, Atmospheric Chemistry and Physics, 16, 8521–8538, https://doi.org/10.5194/acp-16-8521-2016, 2016.

Casado, M., Landais, A., Picard, G., Münch, T., Laepple, T., Stenni, B., Dreossi, G., Ekaykin, A., Arnaud, L., Genthon, C., Touzeau, A., Masson-Delmotte, V., and Jouzel, J.: Archival processes of the water stable isotope signal in East Antarctic ice cores, The Cryosphere, 12, 1745–1766, https://doi.org/10.5194/tc-12-1745-2018, 2018.

Casado, M., Münch, T., and Laepple, T.: Climatic information archived in ice cores: impact of intermittency and diffusion on the recorded isotopic signal in Antarctica, Climate of the Past, 16, 1581–1598, https://doi.org/10.5194/cp-16-1581-2020, 2020.

Cauquoin, A. and Werner, M.: High-Resolution Nudged Isotope Modeling With ECHAM6-Wiso: Impacts of Updated Model Physics and ERA5 Reanalysis Data, Journal of Advances in Modeling Earth Systems, 13, https://doi.org/10.1029/2021MS002532, 2021.

Cauquoin, A., Werner, M., and Lohmann, G.: Water isotopes – climate relationships for the mid-Holocene and preindustrial period simulated with an isotope-enabled version of MPI-ESM, Climate of the Past, 15, 1913–1937, https://doi.org/10.5194/cp-15-1913-2019, 2019.

Craig, H.: Isotopic variations in meteoric waters, Science, 133, 1702–1703, publisher: American Association for the Advancement of Science, 1961.

Ding, Q., Schweiger, A., L'Heureux, M., Battisti, D., Po-Chedley, S., Johnson, N., Blanchard-Wrigglesworth, E., Harnos, K., Zhang, Q., Eastman, R., and Steig, E.: Influence of high-latitude atmospheric circulation changes on summertime Arctic sea ice, Nature Climate Change, 7, 289–295, https://doi.org/10.1038/nclimate3241, 2017.

Ekaykin, A. A., Lipenkov, V. Y., Barkov, N. I., Petit, J. R., and Masson-Delmotte, V.: Spatial and temporal variability in isotope composition of recent snow in the vicinity of Vostok station, Antarctica: implications for ice-core record interpretation, Annals of Glaciology, 35, 181–186, https://doi.org/10.3189/172756402781816726, 2002.

Favier, V., Agosta, C., Parouty, S., Durand, G., Delaygue, G., Gallée, H., Drouet, A.-S., Trouvilliez, A., and Krinner, G.: An updated and quality controlled surface mass balance dataset for Antarctica, The Cryosphere, 7, 583–597, https://doi.org/10.5194/tc-7-583-2013, 2013.

Fogt, R. L., Goergens, C. A., Jones, M. E., Witte, G. A., Lee, M. Y., and Jones, J. M.: Antarctic station-based seasonal pressure reconstructions since 1905: 1. Reconstruction evaluation, Journal of Geophysical Research: Atmospheres, 121, 2814–2835, https://doi.org/10.1002/2015JD024564, 2016.

Goursaud, S., Masson-Delmotte, V., Favier, V., Preunkert, S., Fily, M., Gallée, H., Jourdain, B., Legrand, M., Magand, O., Minster, B., and Werner, M.: A 60-year ice-core record of regional climate from Adélie Land, coastal Antarctica, The Cryosphere, 11, 343–362, https://doi.org/10.5194/tc-11-343-2017, 2017.

Goursaud, S., Masson-Delmotte, V., Favier, V., Orsi, A., and Werner, M.: Water stable isotope spatio-temporal variability in Antarctica in 1960–2013: observations and simulations from the ECHAM5-wiso atmospheric general circulation model, Climate of the Past, 14, 923–946, https://doi.org/10.5194/cp-14-923-2018, 2018.

Goursaud, S., Masson-Delmotte, V., Favier, V., Preunkert, S., Legrand, M., Minster, B., and Werner, M.: Challenges associated with the climatic interpretation of water stable isotope records from a highly resolved firn core from Adélie Land, coastal Antarctica, The Cryosphere, 13, 1297–1324, https://doi.org/10.5194/tc-13-1297-2019, 2019.

Hersbach, H., Bell, B., Berrisford, P., Hirahara, S., Horányi, A., Muñoz-Sabater, J., Nicolas, J., Peubey, C., Radu, R., Schepers, D., et al.: The ERA5 global reanalysis, Quarterly Journal of the Royal Meteorological Society, 146, 1999–2049, 2020.

International Atomic Energy Agency: Reference Sheet for International Measurement Standards, Tech. rep., https://nucleus.iaea.org/rpst/documents/VSMOW_SLAP.pdf, 2006.

Jouzel, J., Masson-Delmotte, V., Cattani, O., Dreyfus, G., Falourd, S., Hoffmann, G., Minster, B., Nouet, J., Barnola, J. M., Chappellaz, J., Fischer, H., Gallet, J. C., Johnsen, S., Leuenberger, M., Loulergue, L., Luethi, D., Oerter, H., Parrenin, F., Raisbeck, G., Raynaud, D., Schilt, A., Schwander, J., Selmo, E., Souchez, R., Spahni, R., Stauffer, B., Steffensen, J. P., Stenni, B., Stocker, T. F., Tison, J. L., Werner, M., and Wolff, E. W.: Orbital and Millennial Antarctic Climate Variability over the Past 800,000 Years, Science, 317, 793–796, https://doi.org/10.1126/science.1141038, 2007.

Jouzel, J., Delaygue, G., Landais, A., Masson-Delmotte, V., Risi, C., and Vimeux, F.: Water isotopes as tools to document oceanic sources of precipitation: Water Isotopes and Precipitation Origin, Water Resources Research, 49, 7469–7486, https://doi.org/10.1002/2013WR013508, 2013.

Kurita, N., Hirasawa, N., Koga, S., Matsushita, J., Steen-Larsen, H. C., Masson-Delmotte, V., and Fujiyoshi, Y.: Identification of air masses responsible for warm events on the East Antarctic coast, SOLA, 12, 307–313, publisher: Meteorological Society of Japan, 2016.

Laepple, T., Hörhold, M., Münch, T., Freitag, J., Wegner, A., and Kipfstuhl, S.: Layering of surface snow and firn at Kohnen Station, Antarctica: Noise or seasonal signal?: Layering of Antarctic Surface Firn, Journal of Geophysical Research: Earth Surface, 121, 1849–1860, https://doi.org/10.1002/2016JF003919, 2016.

Laepple, T., Münch, T., Casado, M., Hoerhold, M., Landais, A., and Kipfstuhl, S.: On the similarity and apparent cycles of isotopic variations in East Antarctic snow pits, The Cryosphere, 12, 169–187, https://doi.org/10.5194/tc-12-169-2018, 2018.

Lagarias, J. C., Reeds, J. A., Wright, M. H., and Wright, P. E.: Convergence Properties of the Nelder–Mead Simplex Method in Low Dimensions, SIAM Journal on Optimization, 9, 112–147, https://doi.org/10.1137/S1052623496303470, 1998.

LeGrande, A. N. and Schmidt, G. A.: Global gridded data set of the oxygen isotopic composition in seawater, Geophysical Research Letters, 33, L12 604, https://doi.org/10.1029/2006GL026011, 2006.

Leroy-Dos Santos, C., Casado, M., Prié, F., Jossoud, O., Kerstel, E., Kassi, S., Fourré, E., Landais, A., and others: A dedicated robust instrument for water vapor generation at low humidity for use with a laser water isotope analyzer in cold and dry polar regions., Atmospheric Measurement Techniques Discussions, pp. 1–17, https://doi.org/https://doi.org/10.5194/amt-2020-345, publisher: Copernicus GmbH, 2021.

450 Leroy-Dos Santos, C., Masson-Delmotte, V., Casado, M., Fourré, E., Steen-Larsen, H., Maturilli, M., Orsi, A., Berchet, A., Cattani, O., and Minster, B.: A 4.5 year-long record of Svalbard water vapor isotopic composition documents winter air mass origin, Journal of Geophysical Research: Atmospheres, p. e2020JD032681, https://doi.org/https://doi.org/10.1029/2020JD032681, publisher: Wiley Online Library, 2020.

Majoube, M.: Fractionnement en $\delta 18O$ entre la glace et la vapeur d'eau, Journal de Chimie Physique, 68, 625–636, 1971.

455 Marshall, G. J., Fogt, R. L., Turner, J., and Clem, K. R.: Can current reanalyses accurately portray changes in Southern Annular Mode structure prior to 1979?, Climate Dynamics, 59, 3717–3740, https://doi.org/10.1007/s00382-022-06292-3, 2022.

Merlivat, L. and Nief, G.: Fractionnement isotopique lors des changements d'état solide-vapeur et liquide-vapeur de l'eau à des températures inférieures à 0°C, Tellus, 19, 122–127, https://doi.org/10.1111/j.2153-3490.1967.tb01465.x, 1967.

Münch, T. and Laepple, T.: What climate signal is contained in decadal- to centennial-scale isotope variations from Antarctic ice cores?,
460   Climate of the Past, 14, 2053–2070, https://doi.org/10.5194/cp-14-2053-2018, 2018.

Pettré, P., Payan, C., and Parish, T. R.: Interaction of katabatic flow with local thermal effects in a coastal region of Adelie Land, east Antarctica, Journal of Geophysical Research, 98, 10 429, https://doi.org/10.1029/92JD02969, 1993.

Retamales-Muñoz, G., Durán-Alarcón, C., and Mattar, C.: Recent land surface temperature patterns in Antarctica using satellite and reanalysis data, Journal of South American Earth Sciences, 95, 102 304, https://doi.org/10.1016/j.jsames.2019.102304, 2019.

465 Rignot, E., Mouginot, J., Scheuchl, B., van den Broeke, M., van Wessem, M. J., and Morlighem, M.: Four decades of Antarctic Ice Sheet mass balance from 1979–2017, Proceedings of the National Academy of Sciences, 116, 1095–1103, https://doi.org/10.1073/pnas.1812883116, 2019.

Ritter, F., Steen-Larsen, H. C., Werner, M., Masson-Delmotte, V., Orsi, A., Behrens, M., Birnbaum, G., Freitag, J., Risi, C., and Kipfstuhl, S.: Isotopic exchange on the diurnal scale between near-surface snow and lower atmospheric water vapor at Kohnen station, East Antarctica,
470   The Cryosphere, 10, 1647–1663, https://doi.org/10.5194/tc-10-1647-2016, 2016.

Schlosser, E., Anschütz, H., Divine, D., Martma, T., Sinisalo, A., Altnau, S., and Isaksson, E.: Recent climate tendencies on an East Antarctic ice shelf inferred from a shallow firn core network, Journal of Geophysical Research: Atmospheres, 119, 6549–6562, https://doi.org/10.1002/2013JD020818, 2014.

Servettaz, A. P. M., Orsi, A. J., Curran, M. A. J., Moy, A. D., Landais, A., Agosta, C., Winton, V. H. L., Touzeau, A., McConnell, J. R.,
475   Werner, M., and Baroni, M.: Snowfall and Water Stable Isotope Variability in East Antarctica Controlled by Warm Synoptic Events, Journal of Geophysical Research: Atmospheres, 125, https://doi.org/10.1029/2020JD032863, 2020.

Sime, L. C., Lang, N., Thomas, E. R., Benton, A. K., and Mulvaney, R.: On high-resolution sampling of short ice cores: Dating and temperature information recovery from Antarctic Peninsula virtual cores, Journal of Geophysical Research, 116, D20 117, https://doi.org/10.1029/2011JD015894, 2011.

480 Sinclair, K. E., Bertler, N. A., Bowen, M. M., and Arrigo, K. R.: Twentieth century sea-ice trends in the Ross Sea from a high-resolution, coastal ice-core record, Geophysical Research Letters, 41, 3510–3516, publisher: Wiley Online Library, 2014.

Smith, R. B. and Evans, J. P.: Orographic Precipitation and Water Vapor Fractionation over the Southern Andes, Journal of Hydrometeorology, 8, 3–19, https://doi.org/10.1175/JHM555.1, 2007.

Steen-Larsen, H. C., Sveinbjörnsdottir, A. E., Peters, A. J., Masson-Delmotte, V., Guishard, M. P., Hsiao, G., Jouzel, J., Noone, D., Warren, J. K., and White, J. W. C.: Climatic controls on water vapor deuterium excess in the marine boundary layer of the North Atlantic based on 500 days of in situ, continuous measurements, Atmospheric Chemistry and Physics, 14, 7741–7756, https://doi.org/10.5194/acp-14-7741-2014, 2014.

Steen-Larsen, H. C., Risi, C., Werner, M., Yoshimura, K., and Masson-Delmotte, V.: Evaluating the skills of isotope-enabled general circulation models against in situ atmospheric water vapor isotope observations: Evaluating Isotope-Enabled GCMs, Journal of Geophysical Research: Atmospheres, 122, 246–263, https://doi.org/10.1002/2016JD025443, 2017.

Stenni, B., Buiron, D., Frezzotti, M., Albani, S., Barbante, C., Bard, E., Barnola, J. M., Baroni, M., Baumgartner, M., Bonazza, M., Capron, E., Castellano, E., Chappellaz, J., Delmonte, B., Falourd, S., Genoni, L., Iacumin, P., Jouzel, J., Kipfstuhl, S., Landais, A., Lemieux-Dudon, B., Maggi, V., Masson-Delmotte, V., Mazzola, C., Minster, B., Montagnat, M., Mulvaney, R., Narcisi, B., Oerter, H., Parrenin, F., Petit, J. R., Ritz, C., Scarchilli, C., Schilt, A., Schüpbach, S., Schwander, J., Selmo, E., Severi, M., Stocker, T. F., and Udisti, R.: Expression of the bipolar see-saw in Antarctic climate records during the last deglaciation, Nature Geoscience, 4, 46–49, https://doi.org/10.1038/ngeo1026, 2011.

Stenni, B., Curran, M. A. J., Abram, N. J., Orsi, A., Goursaud, S., Masson-Delmotte, V., Neukom, R., Goosse, H., Divine, D., van Ommen, T., Steig, E. J., Dixon, D. A., Thomas, E. R., Bertler, N. A. N., Isaksson, E., Ekaykin, A., Werner, M., and Frezzotti, M.: Antarctic climate variability on regional and continental scales over the last 2000 years, Climate of the Past, 13, 1609–1634, https://doi.org/10.5194/cp-13-1609-2017, 2017.

Stevens, B., Giorgetta, M., Esch, M., Mauritsen, T., Crueger, T., Rast, S., Salzmann, M., Schmidt, H., Bader, J., Block, K., and others: Atmospheric component of the MPI-M Earth system model: ECHAM6, Journal of Advances in Modeling Earth Systems, 5, 146–172, publisher: Wiley Online Library, 2013.

Tremoy, G., Vimeux, F., Cattani, O., Mayaki, S., Souley, I., and Favreau, G.: Measurements of water vapor isotope ratios with wavelength-scanned cavity ring-down spectroscopy technology: new insights and important caveats for deuterium excess measurements in tropical areas in comparison with isotope-ratio mass spectrometry: Measuring tropical water vapor isotope ratios using WS-CRDS, Rapid Communications in Mass Spectrometry, 25, 3469–3480, https://doi.org/10.1002/rcm.5252, 2011.

Vega, C. P., Schlosser, E., Divine, D. V., Kohler, J., Martma, T., Eichler, A., Schwikowski, M., and Isaksson, E.: Surface mass balance and water stable isotopes derived from firn cores on three ice rises, Fimbul Ice Shelf, Antarctica, The Cryosphere, 10, 2763–2777, https://doi.org/10.5194/tc-10-2763-2016, 2016.

Wang, L., Ceriotti, M., and Markland, T. E.: Quantum kinetic energy and isotope fractionation in aqueous ionic solutions, Physical Chemistry Chemical Physics, publisher: Royal Society of Chemistry, 2020.

Wang, Y., Ding, M., Reijmer, C. H., Smeets, P. C. J. P., Hou, S., and Xiao, C.: The AntSMB dataset: a comprehensive compilation of surface mass balance field observations over the Antarctic Ice Sheet, Earth System Science Data, 13, 3057–3074, https://doi.org/10.5194/essd-13-3057-2021, 2021.